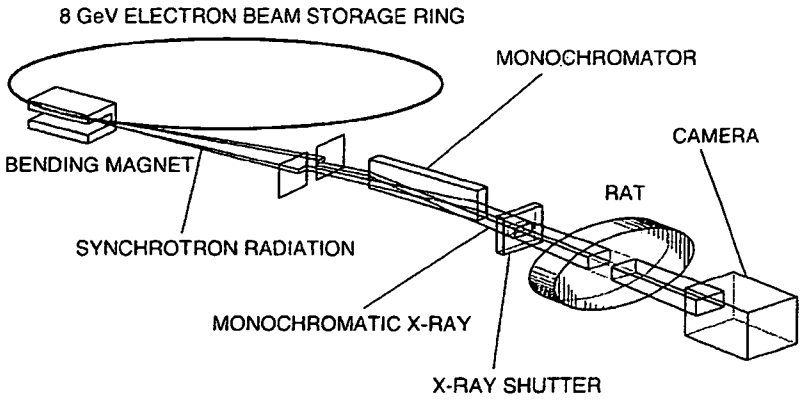

Fig. 7 – Schematic presentation of the experimental setup. Synchrotron radiation is generated by bending the path of electrons at relativistic speeds using a bending magnet. The storage ring maintains the electron beam for many hours. A single silicon crystal selects a single-energy synchrotron radiation. The digital images were acquired through analog-to-digital conversion.

tions of sodium pentobarbital (10 mg/kg). The bilateral common carotid arteries (CCA) were isolated from surrounding tissues through a midline neck incision and silk ligatures were placed loosely around them. Femoral artery and vein catheters were inserted to monitor ABP to measure arterial blood gases (i-STAT, Abbott Laboratories), minerals (sodium and potassium) (i-STAT, Abbott Laboratories) and hematocrit (i-STAT, Abbott Laboratories) and for infusion of anesthetics. Another arterial catheter (PE-50) was placed in the left extra carotid artery for angiography. A temperature sensor (ATB-1100, Nihon Kohden) was inserted into a temporal muscle. The duration of the whole preparation was 1 h from the start of anesthesia to induction of global ischemia.

4.4. *Global ischemia*

Each rat was placed in front of the MSR angiography system on a handmade stereotaxic device to which the head of the rat was certainly fixed by holding both external acoustic meatuses and the incisor in place. The arterial catheter was connected to a pressure transducer (BSM-2301, Nihon Kohden) for the continuous recording of ABP. The body temperature was kept at 37 °C by a blanket and heater (ATB-1100, Nihon Kohden). Global ischemia was induced by occlusion of the bilateral CCA by tightening the silk sutures. Completion of ischemia was checked by the appearance of mydriasis. After 10 min of ischemia, reperfusion was performed by release of the silk sutures. Microangiography was performed before occluding the bilateral CCA, and 1, 5, 10, 15, 20 and 30 min after releasing the silk ligatures by a bolus injection of 0.3 ml of the contrast medium iopamidol, a nonionic water-soluble contrast medium (iodine concentration of 370 mg/ml; Nihon Schering K.K.).

Since each rat had to be manipulated when releasing the silk ligatures of the bilateral CCA, there was a possibility that the rat might shift from the control position. Therefore, the rat was re-positioned by reconfirming the rat's skull image on the camera within 5 min after releasing the ligatures, but not 1 min after releasing the ligatures because of a lack of enough time.

4.5. *Vessel diameter measurement*

Using the NIH Image Device, the microvessel caliber was measured using a 100-μm diameter as the standard. The vascular caliber of the internal carotid artery (ICA) immediately before it branched off the posterior cerebral artery, in the horizontal region of the middle cerebral artery (MCA) immediately after it branched from the ICA, and in the pial arterioles (PA) and striate arteries (SA) immediately after they branched off. The diameters of the PA and SA that were clearly observed on all images were measured (Fig. 2).

Confirming good visualization of the respective vessels in all images, we outlined the region including each respective vessel in each image and converted the gray scale image to an image consisting of only black and white pixels. Then we measured the caliber of the respective vessels. In the case of ICA and MCA, calibers of three different portions that were a few pixels apart from each other were measured. In the case of the PA and SA, calibers of two to four predetermined vessels of the PA and SA were measured.

4.6. *Statistical analysis*

The changes with time are expressed as the means ± SD. The mean basal value was calculated in all vessels. A statistical analysis was performed using the paired t-test. The first value was taken as the control value. Values of $p<0.05$ were considered to be significant.

Acknowledgment

The synchrotron radiation experiments were performed in the BL28B2 experimental unit at SPring-8 with the approval of the Japan Synchrotron Radiation Research Institute (Proposal Nos. 2003B0090, 2004A0128 and 2004B0622).

REFERENCES

Bär, T., 1978. Morphometric evaluation of capillaries in different laminae of rat cerebral cortex by automatic image analysis: changes during development and aging. In: Cervos-Navarro, J. (Ed.), Advances in Neurology. Raven Press, New York, pp. 1–9.

del Zoppo, G.J., et al., 1991. Polymorphonuclear leukocytes occlude capillaries following middle cerebral artery occlusion and reperfusion in baboons. Stroke 22 (10), 1276–1283.

del Zoppo, G.J., von Kummer, R., Hamann, G.F., 1998. Ischaemic damage of brain microvessels: inherent risks for thrombolytic treatment in stroke. J. Neurol. Neurosurg. Psychiatry 65 (1), 1–9.

Garcia, J.H., Liu, K.F., Ho, K.L., 1995. Neuronal necrosis after middle cerebral artery occlusion in Wistar rats progresses at different time intervals in the caudoputamen and the cortex. Stroke 26 (4), 636–643.

Ginsberg, M.D., 1997. The new language of cerebral ischemia. Am. J. Neuroradiol. 18 (8), 1435–1445.

Kidoguchi, K., et al., 2006. In vivo X-ray angiography in the mouse brain using synchrotron radiation. Stroke 37 (7), 1856–1861.

Kontos, H.A., et al., 1978. Responses of cerebral arteries and arterioles to acute hypotension and hypertension. Am. J. Physiol. 234 (4), H371–H383.

Liachenko, S., Tang, P., Hamilton, R.L., Xu, Y., 2001. Regional dependence of cerebral reperfusion after circulatory arrest in rats. J. Cereb. Blood Flow Metab. 23 (11), 1320–1329.

Marchal, G., Young, A.R., Baron, J.C., 1999. Early postischemic hyperperfusion: pathophysiologic insights from positron emission tomography. J. Cereb. Blood Flow Metab. 19 (5), 467–482.

Ohta, H., et al., 2004. Appearance of early venous filling during intra-arterial reperfusion therapy for acute middle cerebral artery occlusion. Stroke 35 (4), 893–898.

Pinard, E., Engrand, N., Seylaz, J., 2000. Dynamic cerebral microcirculatory changes in transient forebrain ischemia in rats: involvement of type 1 nitric oxide synthase. J. Cereb. Blood Flow Metab. 20 (12), 1648–1658.

Pulsinelli, W.A., Brierley, J.B., 1979. A new model of bilateral hemispheric ischemia in the unanesthetized rat. Stroke 10 (3), 267–272.

Pulsinelli, W.A., Brierley, J.B., Plum, F., 1982. Temporal profile of neuronal damage in a model of forebrain ischemia. Ann. Neurol. 11 (5), 491–498.

Tokiya, R., et al., 2004. Observation of microvasculatures in athymic nude rat transplanted tumor using synchrotron radiation microangiography system. Acad. Radiol. 11 (9), 1039–1046.

Umetani, K., et al., 2002. Synchrotron radiation coronary microangiography in isolated perfused rat heart for evaluation of coronary vascular response. Proceedings of 2002 IEEE International Symposium on Biomedical Imaging: Macro to Nano, pp. 561–564.

Villringer, A., et al., 1989. Confocal laser microscopy to study microcirculation on the rat brain surface in vivo. Brain Res. 504 (1), 159–160.

Proceedings of the 29th Annual International
Conference of the IEEE EMBS
Cité Internationale, Lyon, France
August 23-26, 2007.

In Vivo Cerebral Artery Microangiography in Rat and Mouse Using Synchrotron Radiation Imaging System

Keiji Umetani, Keiji Kidoguchi, Akitsugu Morishita, Ximena-Sayuri Oizumi, Masahiro Tamaki, Haruo Yamashita, Takashi Sakurai, and Takeshi Kondoh

Microangiography with spatial resolution in the micrometer range was carried out to depict vascular responses of the cerebral artery and arterioles in rats and mice using a real-time imaging system and a third generation synchrotron radiation source at SPring-8. An X-ray direct-conversion type detector with 6-μm spatial resolution was developed for real-time biomedical imaging. The X-ray image is converted directly into an electrical signal in the photoconductive layer without image blurring. In synchrotron radiation radiography, a long source-to-object distance and a small source spot can produce high-resolution images. Microangiographic images were obtained without image blurring and were stored in a digital frame memory system with a 1024 × 1024-pixel, 10-bit format. In imaging experiments, vasoconstriction and vasodilatation of small cerebral arteries were visualized in response to hypercapnia, hemorrhagic hypotension, and vasoactive agents after iodine contrast agent injection into the carotid artery.

I. Introduction

MEDICAL imaging using synchrotron radiation has been investigated since intravenous coronary angiography research was begun at the end of 1970s. This safe intravenous angiography technique is useful in place of conventional selective coronary arteriography. Research groups in several synchrotron radiation facilities have improved imaging systems for human studies [1–6]. In addition to intravenous coronary angiography, an intra-arterial microangiography system was developed at the Photon Factory for laboratory animal studies to obtain high-resolution images of small blood vessels: the penetrating transmural coronary arteries [7] and vasodilatation of the arterial circle of cerebrum and its branches [8] in dogs, collateral microvessels following therapeutic angiogenesis in rats [9], and tumor-derived angiogenic vessels in mice [10].

In place of synchrotron radiation, an X-ray generator with a small focal spot has been employed for microangiography using an X-ray direct-conversion type VIDICON camera as a two-dimensional high-resolution detector [11,12]. However, the X-ray generator system has limited capability for displaying images of blood vessels smaller than 50-μm diameter: images cannot be magnified without focal-spot blurring. Furthermore, a conventional diagnostic angiography system incorporating an X-ray image intensifier and a video camera is not intended for detection of vessels smaller than 200 μm diameter because it is designed for large-field digital angiographic imaging with a 1024 × 1024-pixel format [7].

At SPring-8, a digital microangiography system with spatial resolution as high as 6 μm was developed using an X-ray direct-conversion type detector incorporating an X-ray SATICON pickup tube for depiction of tumor-derived angiogenic vessels in a rabbit model of cancer [13]. The imaging system was also applied to clarify the basal tone and microvascular reactivity in endothelial NO synthase (eNOS)-overexpressing transgenic mice [14].

For this study, we performed cerebral microangiography in rats and mice and particularly undertook radiographical evaluation of changes in small arteries that had not been observed previously. Small arteries branching directly from major trunk vessels, known as perforators, supply arterial blood to the basal nucleus. These perforators are important arteries when considering the effects of systemic disease on cerebral vessels. Vasoconstriction and vasodilatation of the small cerebral arteries were visualized in response to hypercapnia, hemorrhagic hypotension, and vasoactive agents after injection of iodine contrast agent into the carotid artery [15,16].

II. Imaging System

A. Synchrotron Radiation

A useful source of synchrotron radiation is a storage ring, which maintains an electron beam at relativistic speeds in a closed trajectory for many hours using bending magnets. By bending the path of electrons at relativistic speeds, X-rays are emitted at each bending magnet in a direction tangential to beam trajectory. Fig. 1 shows an experimental arrangement at the SPring-8 BL28B2 beamline for X-ray imaging using monochromatic synchrotron radiation X-rays. Microangiographic imaging for depiction of tumor-derived angiogenic vessels in rabbits [13] and microvascular reactivity in transgenic mice [14] were performed at the BL20B2 beamline. Cerebral microangiographic imaging, however, was carried out at the BL28B2 because this beamline, employing a single crystal monochromator,

Manuscript received March 29, 2007. This study was supported in part by a grant-in-aid for scientific research ((C) (18500359)) to K. Umetani from the Ministry of Education, Science, Sports, and Culture of Japan.

K. Umetani is with Japan Synchrotron Radiation Research Institute, Sayo-gun, Hyogo 679-5198, Japan (corresponding author to provide phone: +81-791-58-0833; fax: +81-791-58-2512; e-mail: umetani@spring8.or.jp).

K. Kidoguchi, A. Morishita, X.-S. Oizumi, M. Tamaki, T. Sakurai, and T. Kondoh are with Kobe University Graduate School of Medicine, Kobe 650-0017, Japan.

H. Yamashita is with Kobe University Hospital, Kobe 650-0017, Japan.

1-4244-0788-5/07/$20.00 ©2007 IEEE

produces higher-flux X-rays than those at the BL20B2, which uses a double-crystal monochromator.

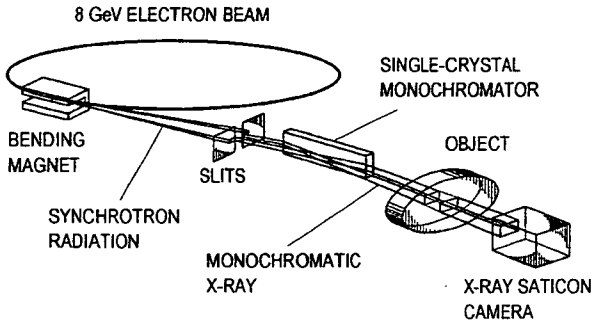

Fig. 1. An illustration of an experimental arrangement for synchrotron radiation microangiography.

Synchrotron radiation generated by bending magnets produces a fan-shaped beam and has a broad and continuous spectrum from infrared to the X-ray region. The single crystal monochromator selects a single energy of synchrotron radiation. Consequently, X-rays with a small energy bandwidth are used for imaging. A rotating-disk X-ray shutter, which is situated between the monochromator and the object, produces pulsed monochromatic X-rays (Fig. 1). The shutter consists of two disks with radial slots rotating about an axis parallel to the X-ray beam. The radial slot width can be changed to adjust the duration of X-ray pulses according to the rotation of one disk with another one. A large amount of disk metal is used to block the beam, resulting in considerably higher attenuation of X-rays, while maintaining low inertia in the disks. The disks rotate to match timing with synchronous signals of a video camera.

Pulsed monochromatic X-rays transmitted through the object are detected using the X-ray direct-conversion type detector, which incorporates the X-ray SATICON pickup tube. The distance between the point-source in the bending magnet and the detector was about 46 m. A nearly parallel X-ray beam was used for imaging without image blur because of the small size X-ray source and the extremely long source-to-object distance. The storage ring was operated at 8 GeV electron beam energy and the beam current was 100 mA. Monochromatic X-ray energy was adjusted to 33.2 keV, which was slightly above the iodine K-edge energy to produce the highest contrast image of the iodine contrast agent. X-ray flux at the object position was ca. 1×10^{10} photons/mm^2/s in imaging experiments.

B. Real-Time Detector

The camera system shown in Fig. 2 comprises a camera head incorporating the X-ray SATICON pickup tube and a camera control unit with an analog-to-digital converter for digital signal output. X-rays enter the SATICON tube through an aluminum window. Fig. 3 shows that absorbed X-rays in the photoconductive layer are converted directly into electron-hole pairs. Charge carriers generated by X-rays are transported across the photoconductive layer by an electric field. Then, a charge-density pattern is formed on the photoconductive layer surface. The electrostatic image on the surface is read out by a scanning beam of low-velocity electrons to produce a video signal. In Fig. 3, X-ray absorption depends on the photoconductive layer thickness. Thickness of amorphous selenium is 25 μm, yielding a detection efficiency of 14.2% for 33.2 keV X-rays.

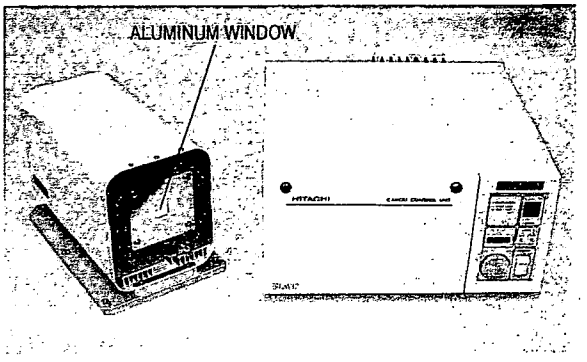

Fig. 2. Photograph of the X-ray SATICON camera system consisting of a camera head (left) and a camera control unit (right).

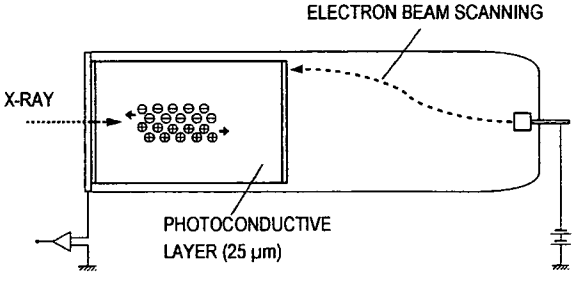

Fig. 3. Schematic cross-section of the SATICON tube. The tube is a glass cylinder maintained under vacuum; the front end of the tube is a flat plate with a diameter of 1 inch, the inside of which is coated with a 25-μm photoconductive material.

In a normal imaging mode with the detector's input field of view of 9.5 mm × 9.5 mm, an equivalent pixel size is 9.5 μm in the case of a 1024 × 1024-pixel format. On the other hand, in zoom imaging modes, the input fields are, respectively, 7.0 mm × 7.0 mm and 4.5 mm × 4.5 mm with pixel size of 7.0 and 4.5 μm. The camera can take sequential images at a maximum speed of 30 images per second. Then the image signals are converted to digital data with the 1024 × 1024-pixel and 10-bit format using an analog-to-digital converter installed in the camera control unit shown in Fig. 2. Digital images are stored in 2 GB RAM of a custom-designed frame memory system after analog-to-digital conversion. Image storage is synchronized with electron-beam scanning

in the pickup tube. A personal computer system controls the entire imaging system, including the camera control unit and the frame memory system.

C. *Microangiography*

Performance of the direct-conversion type detector was evaluated by taking images of a custom-designed gold resolution chart. The chart thickness was 5 μm; the bar pattern widths were 5.0–12.1 μm. After that, male 6-month-old rats weighing 450–600 g and male 10–12-week-old mice weighing 26–29 g were used for microangiographic imaging experiments.

The animals were anesthetized using sodium pentobarbital intraperitoneally. The right external carotid artery was cannulated in the retrograde direction, with the top of the cannula placed close to the common carotid artery so that all the injected contrast agent went into the common carotid artery without affecting the normal blood flow in the internal carotid artery. The rats and mice were held rigidly on a frame with a specially shaped head holder and ear bars. The frame was then fixed vertically to the X-ray beam to obtain axial views of the cerebral arteries.

All animal experiments conformed to the SPring-8 Guide for Care and Use of Laboratory Animals, and all animal experiments were conducted according to the guidelines for animal experiments at Kobe University Graduate School of Medicine.

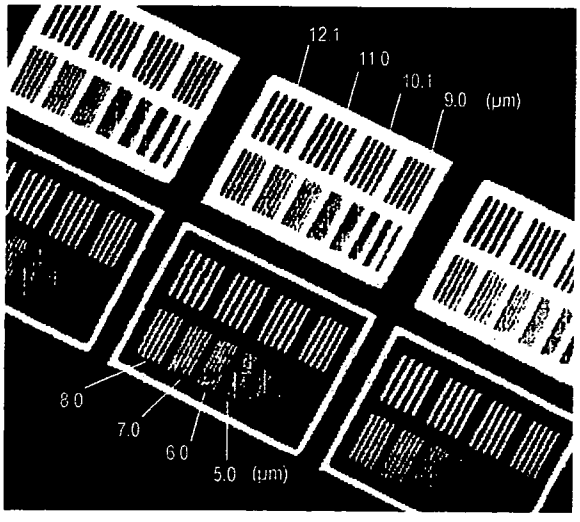

Fig. 4. X-ray image of the central area of the 5-μm-thick chart. Numerical values show bar widths. The limiting spatial resolution is around 6.0 μm.

III. Results and Discussion

An X-ray image of the chart with micrometer-scale bar patterns was obtained in the zoom-imaging mode of the detector with the 4.5 mm × 4.5 mm field of view at an X-ray energy of 20.0 keV. Fig. 4 shows an image of the 5-μm-thick chart; the 6.0-μm-wide bars are visible. The limiting spatial resolution is about 6.0 μm in the zoom imaging mode. The 6.0 μm bar width is comparable to the capillary blood vessels' size. Images of the capillaries are obtainable at an X-ray energy of 33.2 keV just above the iodine K-edge energy to produce the highest contrast image of the iodine contrast agent if capillaries are opacified using a high-density contrast agent. However, the contrast agent is diluted substantially in the blood flow.

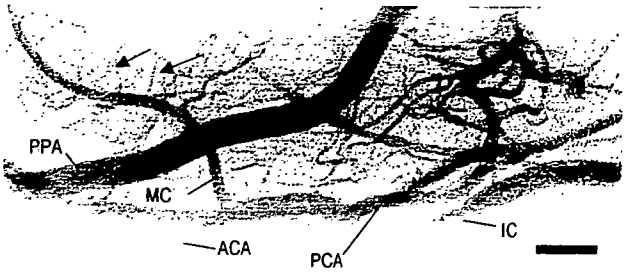

Fig. 5. Synchrotron radiation angiography of a rat showing the anatomy of the cerebral arteries in the brain hemisphere. Black arrows indicate perforating arteries; MCA, middle cerebral artery; ICA, internal carotid artery; ACA, anterior cerebral artery; PCA, posterior cerebral artery; PPA, pterygopalatine artery. Selective imaging was performed in the ICA territory. The scale bar shows 1 mm.

Angiography was performed selectively in the internal carotid artery (ICA) territory. A representative image of the rat cerebral arteries in Fig. 5 was obtained in the normal imaging mode of the detector with the 9.5 mm × 9.5 mm field of view. The smallest detectable vessels were branches of the middle cerebral artery (MCA), which were ca. 30-μm diameter. We confirmed the right ICA, the anterior cerebral artery (ACA), the posterior cerebral artery (PCA), and the pterygopalatine artery (PPA) entirely. We specifically examined the large perforators, which were mostly found arising from the middle cerebral artery trunk. Vasoconstriction and vasodilatation of the large perforators were visualized in response to hypercapnia, hemorrhagic hypotension, and vasoactive agents after iodine contrast agent injection into the carotid artery [15,16].

Fig. 5 depicts a summation result image of 10 consecutive frames in the microangiographic sequence. Original frames, however, were obtained at a rate of 30 frames per second. Image summation was necessary to increase the signal-to-noise ratio and to detect small blood vessels. Furthermore, a temporal subtraction operation was performed for flat-field correction using summation results of 10 consecutive frames acquired before contrast-agent injection. The summation image taken before injection was subtracted from raw images taken after injection to eliminate the superimposed background structure.

We developed a novel cerebral angiography procedure for rats and mice using monochromatic synchrotron radiation X-rays and obtained images of the cerebral perforating arteries for the first time. These results demonstrate the importance of hemodynamic studies in deep brain vessels that had previously been unattainable.

ACKNOWLEDGMENTS

The authors wish to thank Mr. Tadaaki Hirai and Mr. Toshiaki Kawai of Hamamatsu Photonics K.K., Mr. Sadao Takahashi of Hitachi Denshi Techno-System, Ltd., and Mr. Norio Iwanaga of Zenisu Keisoku Inc. for development of the camera and frame memory system. Synchrotron radiation experiments were performed at the SPring-8 BL28B2 beamline with the approval of the Japan Synchrotron Radiation Research Institute (Acceptance Nos. 2002A0079, 2002B0312, 2004A0313, 2004B0767, 2005A0524, and 2005B0675).

REFERENCES

[1] E. Rubenstein, R. Hofstadter, H. D. Zeman, A. C. Thompson, J. N. Otis, G. S. Brown, J. C. Giacomini, H. J. Gordon, R. S. Kernoff, D. C. Harrison, and W. Thomlinson, "Transvenous Coronary Angiography in Human Using Synchrotron Radiation," *Proc. Natl. Acad. Sci. U.S.A.*, vol. 83, pp. 9724-9728, 1987.

[2] W. Thomlinson, "Transvenous Coronary Angiography in Humans," in *Proc. the International School of Physics Enrico Fermi Course CXXVIII, Biomedical Applications of Synchrotron Radiation*, E. Burattini and A. Balerna, Eds. Amsterdam : IOS Press, 1996, pp. 127-153.

[3] W.-R. Dix, W. Graeff, J. Heuer, K. Engelke, H. Jabs, W. Kupper, and K. H. Stellmaschek, "NIKOS II–A System for Noninvasive Coronary Angiography with Synchrotron Radiation," *Rev. Sci. Instrum.*, vol. 60, p. 2260, 1989.

[4] T. Dill, W.-R. Dix, C. W. Hamm, M. Jung, W. Kupper, M. Lohmann, B. Reime, and R. Ventura, "Intravenous Coronary Angiography: Experience in 276 Patients," *Synchrotron Radiation News*, vol. 11(2), pp. 12-20, 1998.

[5] S. Ohtsuka, Y. Sugishita, T. Takeda, Y. Itai, K. Hyodo, and M. Ando, "Dynamic Intravenous Coronary Arteriography Using Synchrotron Radiation and Its Application to the Measurement of Coronary Blood Flow," *Jpn. Circ. J.*, vol. 61(5), pp. 432-440, 1997.

[6] H. Elleaume, S. Fiedler, F. Estève, A. M. Charvet, B. Bertrand, P. Berkvens, G. Berruyer, T. Brochard, G. Le Duc, C. Nemoz, M. Renier, P. Suortti, W. Thomlinson, and J. F. Le Bas, "First Human Transvenous Coronary Angiography at the European Synchrotron Radiation Facility," *Phys. Med. Biol.*, vol. 45, pp. L39-L43, 2000.

[7] H. Mori, K. Hyodo, E. Tanaka, M. Uddin-Mohammed, A. Yamakawa, Y. Shinozaki, H. Nakazawa, Y. Tanaka, T. Sekka, Y. Iwata, S. Handa, K. Umetani, H. Ueki, T. Yokoyama, K. Tanioka, M. Kubota, H. Hosaka, N. Ishikawa, and M. Ando, "Small-Vessel Radiography In Situ with Monochromatic Synchrotron Radiation," *Radiology*, vol. 201, pp. 173-177, 1996.

[8] E. Tanaka, A. Tanaka, T. Sekka, Y. Shinozaki, K. Hyodo, K. Umetani, and H. Mori, "Digitized Cerebral Synchrotron Radiation Angiography: Quantitative Evaluation of the Canine Circle of Willis and its Large and Small Branches," *Am. J. Neuroradiol.*, vol. 20, pp. 801-806, 1999.

[9] S. Takeshita, T. Isshiki, H. Mori, E. Tanaka, K. Eto, Y. Miyazawa, A. Tanaka, Y. Shinozaki, K. Hyodo, M. Ando, M. Kubota, K. Tanioka, K. Umetani, M. Ochiai, T. Sato, and H. Miyashita, "Use of Synchrotron Radiation Microangiography to Assess Development of Small Collateral Arteries in a Rat Model of Hindlimb Ischemia," *Circulation*, vol. 95, pp. 805-808, 1997.

[10] T. Sekka, S. A. Volchikhina, A. Tanaka, M. Hasegawa, Y. Tanaka, Y. Ohtani, T. Tajima, H. Makuuchi, E. Tanaka, Y. Iwata, S. Sato, K. Hyodo, M. Ando, K. Umetani, M. Kubota, K. Tanioka, and H. Mori, "Visualization, Quantification and Therapeutic Evaluation of Angiogenic Vessels in Cancer by Synchrotron Microangiography," *J. Synchrotron Rad.*, vol. 7, pp. 361-367, 2000.

[11] K. Sada, M. Shirai, and I. Ninomiya, "X-ray TV System for Measuring Microcirculation in Small Pulmonary Vessels," *J. Appl. Physiol.*, vol. 59, pp. 1013-1018, 1985.

[12] M. Shirai, S. Ikeda, K.-Y. Min, A. Shimouchi, T. Kawaguchi, and I. Ninomiya, "Segmental Difference in Vasodilatation due to Basal NO Release in In Vivo Cat Pulmonary Vessels," *Respir. Physiol.*, vol. 116, pp. 159-169, 1999.

[13] K. Umetani, T. Yamashita, N. Maehara, R. Tokiya, S. Imai, and Y. Kajihara, "Small-Field Angiographic Imaging of Tumor Blood Vessels in Rabbit Auricle Using X-ray SATICON Camera and Synchrotron Radiation," in *Proc. 25th Annual Int. Conf. of the IEEE Engineering in Medicine and Biology Society*, Cancún, 2003, pp. 978-981.

[14] T. Yamashita, S. Kawashima, M. Ozaki, M. Namiki, M. Shinohara, N. Inoue, K. Hirata, K. Umetani, and M. Yokoyama, "In Vivo Angiographic Detection of Vascular Lesions in Apolipoprotein E-knockout Mice Using a Aynchrotron Radiation Microangiography System," *Circ J.*, vol. 66, pp. 1057–1059. 2002.

[15] K. Kidoguchi, M. Tamaki, T. Mizobe, J. Koyama, T. Kondoh, E. Kohmura, T. Sakurai, K. Yokono, and K. Umetani, "In Vivo X-Ray Angiography in the Mouse Brain Using Synchrotron Radiation," *Stroke*, vol. 37, pp. 1856-1861, 2006.

[16] A. Morishita, T. Kondoh, T. Sakurai, M. Ikeda, A. K. Bhattacharje, S. Nakajima, E. Kohmura, K. Yokono, and K. Umetani, "Quantification of Distension in Rat Cerebral Perforating Arteries," *NeuroReport*, vol. 17, pp. 1549-1553, 2006.

Microscopic X-ray imaging system for biomedical applications using synchrotron radiation

Keiji Umetani*[a], Makito Kobatake[b], Akira Yamamoto[b], Takenori Yamashita[b], Shigeki Imai[b]
[a] Japan Synchrotron Radiation Research Institute, Sayo-cho, Sayo-gun, Hyogo 679-5198, Japan;
[b] Dept. of Diagnostic Radiology, Kawasaki Medical School, Kurashiki, Okayama 701-0192, Japan

ABSTRACT

An X-ray direct-conversion type detector with a spatial resolution of 10-11 μm was developed for real-time biomedical imaging. The detector incorporates the X-ray SATICON pickup tube with a photoconductive target layer of amorphous selenium. For high-resolution imaging, the X-ray image is directly converted into an electric signal in the photoconductive layer without image blur. Microangiography experiments were carried out for depicting angiogenic vessels in a rabbit model of cancer using the direct-conversion detector and a third generation synchrotron radiation source at SPring-8. In synchrotron radiation radiography, a long source-to-object distance and a small source spot can produce high-resolution images. After transplantation of cancer cells into the rabbit auricle, small tumor blood vessels with diameters of 20-30 μm in an immature vascular network produced by angiogenesis were visualized by contrast material injection into the auricular artery at a monochromatic X-ray energy of 33.2 keV just above the iodine K-edge energy. The synchrotron radiation system is a useful tool to evaluate the micro-angioarchitecture of malignant tumors in animal models of cancer for *in vivo* preclinical studies.

Keywords: X-ray SATICON, microangiography, synchrotron radiation, monochromatic X-ray, preclinical study, angiogenesis, malignant tumor

1. INTRODUCTION

Medical imaging using synchrotron radiation has been investigated since dual-energy subtraction coronary angiography was started in 1979 [1]. Differential X-ray absorption by iodine contrast material at energies just above and just below the iodine K-edge energy has been used for high-sensitivity imaging of the diluted contrast material. Research groups at several synchrotron radiation facilities have improved dual-energy imaging systems for human studies [2-5]. Such systems are composed of two single-dimensional line detectors and two fan beams, one just above and the other just below the iodine K-edge energy. For a two-dimensional image, a patient is scanned vertically through the two fan beams and two line detectors.

In Japan, the first human study of intravenous coronary angiography was performed using a combination of one single-energy beam and one two-dimensional detector [6]. In this approach, a monochromatic X-ray beam with a large cross-section size and energies just above the iodine K-edge energy was used to produce two-dimensional images without a patient scan. The two-dimensional detector approach has also been applied to intra-arterial microangiography [7]. Aside from coronary angiography for human studies, the intra-arterial microangiography system has been investigated as a preclinical imaging tool for circulatory disorders and early stage malignant tumors using laboratory animals [8].

An X-ray generator with a small focal spot has been employed for conventional microangiography combined with an X-ray direct-conversion type VIDICON camera as a two-dimensional high-resolution detector [9]. The X-ray generator system, however, has limitations when providing images of small blood vessels with diameters of less than 50 μm because images cannot be magnified without focal spot blurring. In addition, a diagnostic angiography system incorporating an X-ray image intensifier and a video camera is not intended for detection of small vessels having diameters of 200 μm or less because it is designed for large-field digital angiographic imaging with a 1024×1024-pixel format.

At SPring-8, the digital microangiography system with a spatial resolution down to 10-11 μm was developed using a direct-conversion type detector incorporating the X-ray SATICON pickup tube [10]. Microangiography experiments were carried out for depicting angiogenic vessels in a rabbit model of cancer at a monochromatic X-ray energy of 33.2

Sensors, Cameras, and Systems for Scientific/Industrial Applications VIII, edited by Morley M. Blouke,
Proc. of SPIE-IS&T Electronic Imaging, SPIE Vol. 6501, 650112, © 2007 SPIE-IS&T · 0277-786X/07/$18

keV just above the iodine K-edge energy. Sequential images of tumor blood vessels induced by transplanted VX2 cancer cells in the rabbit auricle were obtained after iodine contrast material injection to the auricular artery and then the tumor-induced small blood vessels with diameters of 20-30 μm were visualized.

2. METHODS

2.1 Image detector

The X-ray direct-conversion type SATICON tube consists of a photoconductive target layer of amorphous selenium in Fig. 1. Absorbed X-rays in the photoconductive layer of the tube are directly converted into electron-hole pairs. Charge carriers generated by X-rays are transported across the photoconductive layer by an electric field. Then, a charge-density pattern is formed on the photoconductive layer surface. The electrostatic image on the surface is read out by a scanning beam of low velocity electrons to produce a video signal.

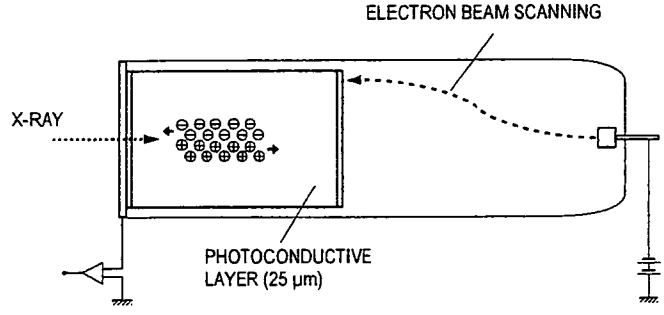

Fig. 1. Schematic cross-section of the X-ray direct-conversion type pickup tube consisting of a photoconductive target layer.

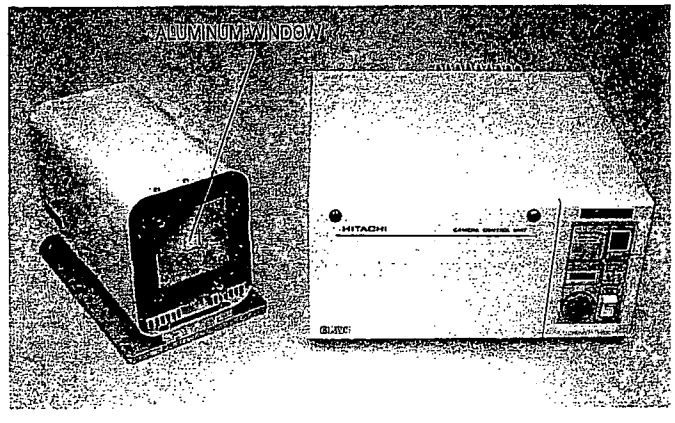

Fig. 2. Photograph of the SATICON camera system: a camera head (left) and a camera control unit (right).

The X-ray direct-conversion type pickup tube was developed in the 1960's using a PbO photoconductive layer. The image detector was combined with a high-power X-ray generator for observation of real-time topography images in material science fields. Photoconductive materials were improved for high-resolution imaging. In place of the PbO photoconductive layer, the X-ray SATICON tube with an amorphous photoconductive Se-As alloy target was developed for use in synchrotron radiation experiments of live topography at the Photon Factory [11]. After that, the direct-conversion camera was much improved through introduction of a high-definition television (HDTV) system, which increased resolution to 1050 scanning lines.

The new X-ray SATICON camera in Fig. 2 for biomedical imaging has identical resolution of 1050 scanning lines. The camera can take images at a maximum speed of 30 images/s. Sequential images were obtained with an input field of view of 9.5 mm × 9.5 mm. Digital images were stored in a digital-image acquisition system after analog-to-digital conversion, synchronizing timing with electron beam scanning in the pickup tube. An equivalent pixel size projected onto the input window was 9.5 μm in the case of the 1024 × 1024-pixel format.

2.2 Imaging system

The medium length bending-magnet beamline BL20B2 at SPring-8 in Fig. 3 is dedicated mainly to basic medical science using biological specimens and small animals. Synchrotron radiation has a broad and continuous spectrum from the infrared to the X-ray region. A double crystal monochromator selects a single energy of synchrotron radiation, and X-rays with a small energy bandwidth are used for imaging. In Fig. 3, the storage ring and the beamline consist of vacuum tubes. The monochromatic X-ray comes out from the vacuum tube into the atmosphere by passing through a beryllium window that is located in the down stream of vertical slits. The X-rays transmitted through the object are detected by the imaging detector.

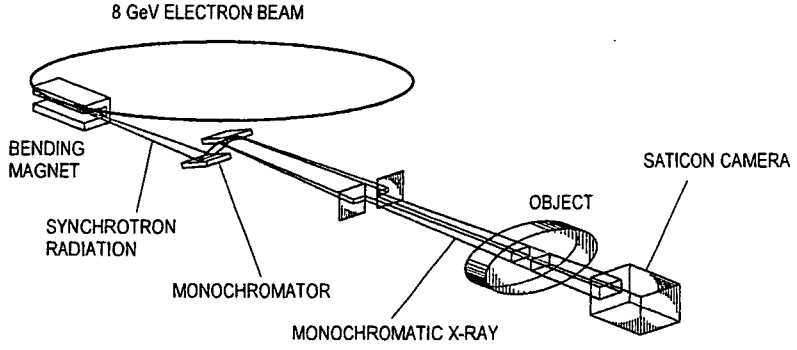

Fig. 3. Illustration of the experimental arrangement at SPring-8 BL20B2 beamline.

The distance between the source point in the bending magnet and the detector was about 210 meters. The nearly parallel X-ray beam was used for imaging without geometrical unsharpness because of the small size of the X-ray source and the very long source-to-object distance. The storage ring was operated at 8 GeV electron beam energy and the beam current was 100 mA. The energy of monochromatic X-ray was adjusted to 33.2 keV just above the iodine K-edge energy to produce the highest contrast image of the iodine contrast material. X-ray flux at the object position was around 4×10^7 photons/mm^2/s.

2.3 In vivo imaging

We conducted an experimental study using rabbit VX2 carcinoma in the rabbit auricle to evaluate growth of tumor-induced small blood vessels. VX2 carcinoma is a rapidly growing solid tumor. The tumor cells are easily transplanted into other rabbits. Japanese white rabbits weighing about 3 kg were used for microangiographic imaging. The rabbits were anesthetized with an intravenous injection of pentobarbital sodium. Then, the VX2 cancer cells were subcutaneously injected into the rabbit auricle.

Microangiography experiments were performed at one, three, and seven days after transplantation. After the rabbit was similarly anesthetized, an intracatheter was inserted into the auricular artery. The rabbit was placed in lateral posture on a stage and the auricle was put in the X-ray field of view. The contrast material used for imaging was 0.8 ml per one injection at a speed of 0.2 ml/s. The contrast material was injected into the auricular artery by an auto injector. The timing of the injection was controlled by the digital-image acquisition system.

Microangiographic images were obtained sequentially at a speed of 5 images/s. The exposure time per image was 0.2 s. Images were stored in the digital-image acquisition system with the 10-bit resolution and 1024 × 1024-pixel format. The

total number of acquired frames was 50 and the total imaging time was 10 s. The animal protocol used was approved by the Animal Care and Use Committee of Kawasaki Medical School. All of our experiments on animals conformed to the SPring-8 Guide for the Care and Use of Laboratory Animals.

3. RESULTS

Performance of the direct-conversion detector was evaluated by taking an image of a spatial resolution chart. We used a specially ordered gold bar chart with up to 8.8-μm-width patterns. The thickness of the gold chart was 23 μm and pattern widths were 8.8-31.4 μm. The limiting spatial resolution was 10-11 μm and nearly equal to 9.5 μm, which is equivalent to Nyquist frequency [10]. A conventional angiography system using an X-ray image intensifier and a video camera has the limiting spatial resolution of around 100 and 200 μm when a circular input field of the X-ray image intensifier is 4.5 and 9 inches in diameter, respectively. Our small-field imaging system using the direct-conversion detector achieved the limiting spatial resolution of 10-11 μm, which is 10-20 times higher resolution than that of the conventional diagnostic system designed for large-field digital angiographic imaging.

A tumor stimulates growth of small blood vessels for feeding the tumor itself. It has been proposed that tumor-induced small blood vessels are an intrinsic part of tumor development and progression. The growth rate of tumors is slow before blood vessel formation and rapid after vessel formation [12,13]. Radiographic depiction of tumor-induced small vessels that feed a space-occupying lesion is a useful tool for preclinical studies of malignant tumors.

Representative images from a microangiographic sequence is shown in Fig. 4. Sequential images of the transplanted tumor were taken at three days after transplantation by the direct-conversion detector after contrast material injection into the auricular artery. Each image in Fig. 4 is a summation result of four consecutive frames in the angiographic sequence. The image summation was needed to reduce quantum noise and to visualize small blood vessels. A temporal subtraction operation was also performed for flat field correction. The summation of four consecutive frames, which were taken just before the contrast material injection, was subtracted from the summation of four iodine injection frames to eliminate the superimposed background structure.

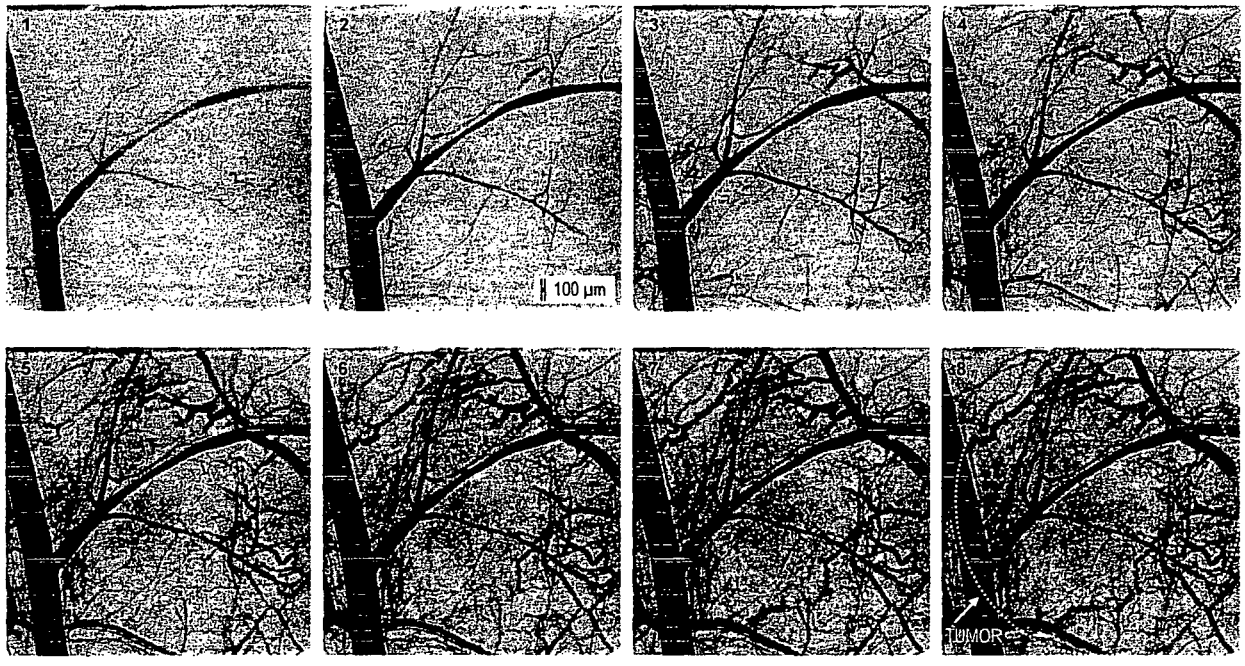

Fig. 4. Sequential images of tumor blood vessels (dotted circle) after iodine injection at three days after tumor transplantation.

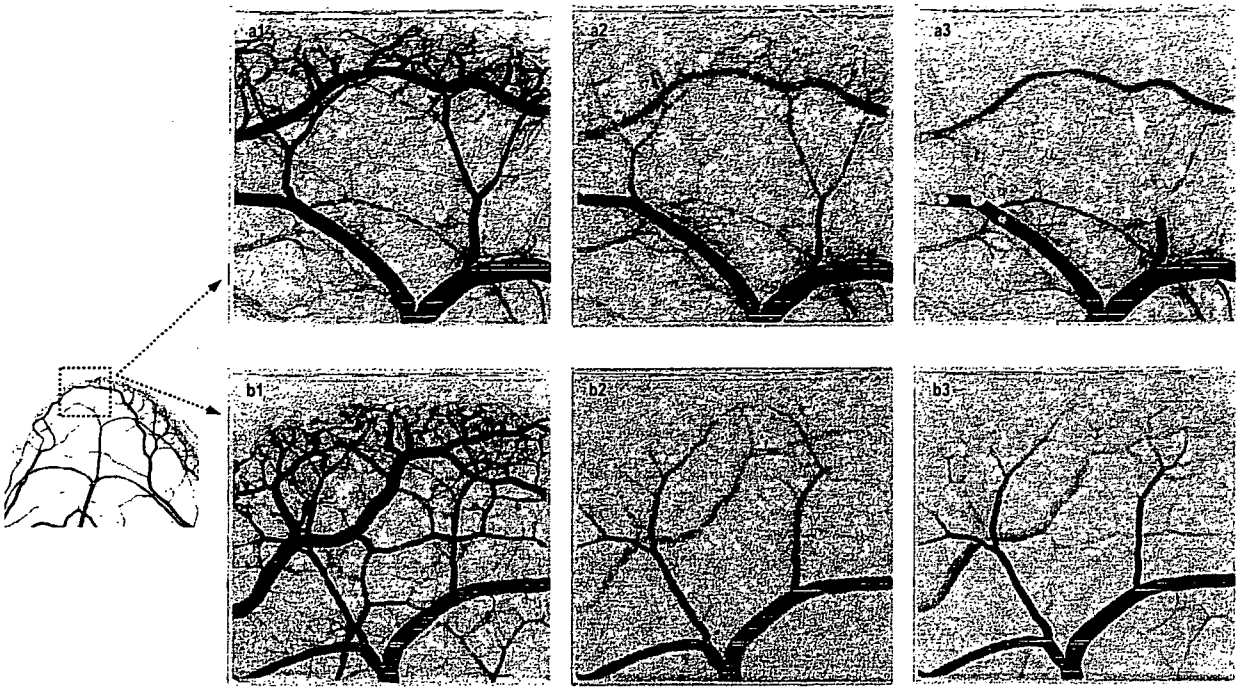

Fig. 5. Two sets of normal blood vessel images in the marginal region of the auricles showing the effects of transcatheter arterial embolization: (a1 and b1) before embolization, (a2 and b2) under embolization, and (a3 and b3) after embolization. Embolization materials are particles with diameters of (a1-a3) 100-300 μm and (b1-b3) 90-180 μm.

Small particles clog small blood vessels and block blood flow to the tumor. Arterial embolization is the selective blocking of arteries by introducing embolization materials to treat certain types of cancer. In this procedure, a mixture of the contrast material and a synthetic material that is designed to occlude the blood vessels was injected for blocking and imaging. We tested two types of particulate embolization materials: polyvinyl alcohol (PVA) particles and trisacryl gelatin microspheres (TGM) with respective diameters of 100-300 μm and 90-180 μm. Figure 5 shows the effect of transcatheter arterial embolization on normal blood vessels in marginal region of the rabbit auricles.

Results of testing the particulate materials with diameters of about 100-300 μm (PVA) and 90-180 μm (TGM) are shown respectively in Fig. 5 (top row) and Fig. 5 (bottom row). The first images were obtained before the embolization procedure (left column), the second ones during the procedure (center column), and the third ones after the procedure (right column). The first and third images in Fig. 5 were taken using a conventional injection material comprising only the contrast material, whereas the second images were taken using a mixture of the contrast material and the embolization material under the procedure.

4. DISCUSSION

At three days after transplantation, the tumor size was 5-6 mm in diameter. In Fig. 4, a dotted circle shows the immature vascular network in the transplanted solid tumor. The first-third images in Fig. 4 mainly show the network of tumor-feeding arteries originating from the first-order branch of the auricular artery; some veins are slightly visible in the top right of the image because of arteriovenous malformations. Small blood vessels of 20-30 μm diameter are depicted in these image. The number of vessels in the solid tumor increased remarkably compared with that of the normal area in the auricle. The tumor derived blood vessels exhibit many irregular veins, which have the characteristic appearance of an undulating shape lacking side branches. The vascular network also shows abnormal staining.

The X-ray generator system with the small focal spot can visualize images of small blood vessels with diameters of more than 50 μm. The synchrotron radiation system, however, can provide images of blood vessels with diameters of 20-30 μm, which is 2-3 times higher detection than that of the X-ray generator system. The detection can improve by the operation of the camera with a zoom imaging mode [10].

In testing of the embolization materials in transcatheter arterial embolization, microangiographic images show the microscopic mechanism of the blood vessel occlusion. In particular, Fig. 5 (top right panel) shows individual PVA particles with 100–300 μm diameter wedging in the auricular artery. Images also illustrate that the levels of occlusion and collateral blood supply were controlled by particle sizes. In Fig. 5 (top right panel), almost all small arteries were blocked with PVA particles (100–300 μm), whereas TGM particles (90–180 μm) did not clog arteries with diameters of more than 100–200 μm in Fig. 5 (bottom right panel).

5. CONCLUSIONS

X-ray imaging with a spatial resolution of 10-11 μm was carried out using the direct-conversion detector and the nearly parallel X-ray beam provided at SPring-8. In synchrotron radiation radiography, the long source-to-object distance and the small source spot can overcome geometric unsharpness. The imaging system can visualize the immature vascular network in the transplanted malignant tumor, and it is useful for the depiction and quantification of angiogenic vessels in the rabbit model of cancer. Furthermore, microangiographic images show the microscopic mechanism of the blood vessel occlusion in testing of the embolization materials in transcatheter arterial embolization. The synchrotron radiation imaging system will be a useful tool for evaluating the micro-angioarchitecture of malignant tumors for preclinical studies.

Before the 1990s, video cameras consisted of a pickup tube to capture images and then the pickup tube has largely been replaced by a charge-coupled device (CCD). Some pickup tube cameras such as the X-ray SATICON camera are still used for special purpose applications in scientific and industrial fields. However, all of the present pickup tubes will be replaced by solid-state image sensors in the near future. The tube is a glass cylinder maintained under vacuum; the front end of the tube is a flat plate, the inside of which is coated with a photosensitive material. The field-of-view limit is imposed by a diameter of the glass cylinder, a standard size of one inch. If an X-ray direct-conversion type solid-state image sensor with spatial resolution in the micrometer range is produced for special purpose applications, the sensor will be able to remove restrictions on the field of view, while retaining temporal and spatial resolution.

ACKNOWLEDGMENTS

The authors would like to thank Mr. Tadaaki Hirai and Mr. Toshiaki Kawai of Hamamatsu Photonics K.K. for development of the X-ray SATICON tube. The authors also thank Mr. Sadao Takahashi of Hitachi Denshi Techno-System, Ltd. for providing the camera system. The authors also thank Mr. Norio Iwanaga of Zenisu Keisoku Inc. for development of the frame memory system.

REFERENCES

1. E. Rubenstein, E. B. Hughes, L. E. Campbell, R. Hofstadter, R. L. Kirk, T. J. Krolicki, J. P. Stone, S. Wilson, H. D. Zeman, W. R. Brody, A. Macovski, and A. C. Thompson, "Synchrotron radiation and its application to digital subtraction angiography," *Proc. SPIE* 314, 42-49 (1981).
2. E. Rubenstein, R. Hofstadter, H. D. Zeman, A. C. Thompson, J. N. Otis, G. S. Brown, J. C. Giacomini, H. J. Gordon, R. S. Kernoff, D. C. Harrison, W. Thomlinson, *Proc. Natl. Acad. Sci. USA.* **83**, 9724-9728 (1986).

3. W. Thomlinson "Transvenous Coronary Angiography in Humans," *Proc. the international School of Physics Enrico Fermi Course CXXVIII, Biomedical Applications of Synchrotron Radiation*, pp. 127-153, IOS Press, Amsterdam (1996).
4. T. Dill, W. -R. Dix, C. W. Hamm, M. Jung, W. Kupper, M. Lohmann, B. Reime, R. Ventura, "Intravenous coronary angiography with synchrotron radiation," *Eur. J. Phys.* **19**, 499-511 (1998).
5. H. Elleaume, S. Fiedler, F. Estève, B. Bertrand, A. M. Charvet, P. Berkvens, G. Berruyer, T. Brochard, G. Le Duc, C. Nemoz, M. Renier, P. Suortti, W. Thomlinson, J. F. Le Bas, "First human transvenous coronary angiography at the European Synchrotron Radiation Facility," *Phys. Med. Biol.* **45**, L39-L43 (2000).
6. S. Ohtsuka, Y. Sugishita, T. Takeda, Y. Itai, J. Tada, K. Hyodo, and M. Ando, "Dynamic intravenous coronary angiography using 2D monochromatic synchrotron radiation," *Br. J. Radiol.* **72**, 24-28 (1999).
7. K. Umetani, H. Ueki, T. Takeda, Y. Itai, H. Mori, E. Tanaka, M. Uddin-Mohammed, Y. Shinozaki, M. Akisada, and Y. Sasaki, "High-spatial-resolution and real-time medical imaging using a high-sensitivity HARPICON camera," *J. Synchrotron Rad.* **5**, 1130-1132 (1998).
8. H. Mori, K. Hyodo, E. Tanaka, M. Uddin-Mohammed, A. Yamakawa, Y. Shinozaki, H. Nakazawa, Y. Tanaka, T. Sekka, Y. Iwata, S. Handa, K. Umetani, H. Ueki, T. Yokoyama, K. Tanioka, M. Kubota, H. Hosaka, N. Ishikawa, and M. Ando, "Small-vessel radiography in situ with monochromatic synchrotron radiation," *Radiology* **201**, 173-177 (1996).
9. K. Sada, M. Shirai, and I. Ninomiya, "X-ray TV system for measuring microcirculation in small pulmonary vessels," *J. Appl. Physiol.* **59**, 1013-1018 (1985).
10. K. Umetani, M. Kobatake, A. Yamamoto, T. Yamashita, S. Imai, Y. Kajihara, "High-resolution, real-time X-ray imaging system using synchrotron radiation for animal studies," *Proc. the 3rd European Medical & Biological Engineering Conference - EMBEC'05*, 263-268 (2005).
11. J. Chikawa, F. Sato, T. Kawamura, T. Kuriyama, T. Yamashita, and N. Goto, "A high-resolution video camera tube for live X-ray topography using synchrotron radiation," *X-ray Instrumentation for the Photon Factory: Dynamic Analysis of Micro Structures in Matter*, S. Hosoya *et al.* (eds.), pp. 145-157, KTK Scientific Publishers, Tokyo (1986).
12. J. Folkman, "What is the evidence that tumors are angiogenesis dependent ?," *J. Natl. Cancer Inst.* **82**, 4-6 (1990).
13. J. Folkman, "Angiogenesis in cancer, vascular, rheumatoid and other disease," *Nat. Med.* 1, 27-31 (1995).

J Appl Physiol 104: 88–96, 2008.
First published October 25, 2007; doi:10.1152/japplphysiol.00610.2007.

Changes in macrovessel pulmonary blood flow distribution following chronic hypoxia: assessed using synchrotron radiation microangiography

Daryl O. Schwenke,[1,2] James T. Pearson,[3] Kenji Kangawa,[1] Keiji Umetani,[4] and Mikiyasu Shirai[5]

[1]*Department of Biochemistry, National Cardiovascular Center Research Institute, Suita, Osaka, Japan;* [2]*Department of Physiology, University of Otago, Dunedin, New Zealand;* [3]*Department of Physiology and Monash Centre for Synchrotron Science, Monash University, Melbourne, Australia;* [4]*Japan Synchrotron Radiation Research Institute, Hyogo, Japan; and* [5]*Faculty of Health Sciences, Hiroshima International University, Hiroshima, Japan*

Submitted 10 June 2007; accepted in final form 22 October 2007

Schwenke DO, Pearson JT, Kangawa K, Umetani K, Shirai M. Changes in macrovessel pulmonary blood flow distribution following chronic hypoxia: assessed using synchrotron radiation microangiography. *J Appl Physiol* 104: 88–96, 2008. First published October 25, 2007; doi:10.1152/japplphysiol.00610.2007.—Structural and functional changes of the pulmonary circulation, particularly during the pathogenesis of pulmonary arterial hypertension (PAH), remain to be fully elucidated. In this study, we utilized monochromatic synchrotron radiation (SR) microangiography to assess changes in pulmonary arteriole blood flow in the intact-chest rat after 4 wk of chronic hypoxia. Sprague-Dawley rats were exposed to normoxia (N-rats) or chronic hypoxia (10% O_2; CH-rats) for 28 days. Rats were anesthetized, and microangiography was performed on the left lung to assess *1*) the branching distribution of pulmonary arteriole blood flow (internal diameter >80 μm) and *2*) dynamic changes in vessel lumen diameter during acute hypoxic (8% O_2 for 4 min) pulmonary vasoconstriction (HPV) before and after β-adrenoceptor blockade (2 mg/kg iv propranolol). Using SR angiography, we observed that the number of opaque third- and fourth-generation vessels (100–300 μm) for CH-rats was significantly fewer than the number for N-rats. The magnitude of HPV was not different between CH-rats and N-rats. β-Adrenoceptor blockade accentuated the HPV in 200- to 300-μm vessels for CH-rats, but even more so in N-rats. However, in CH-rats, β-adrenoceptor blockade also accentuated the HPV in 100- to 200-μm vessels. In summary, we utilized SR to assess gross blood flow changes and functional changes (i.e., HPV) of the pulmonary circulation in PAH. These results highlight the benefits of SR for assessing pulmonary circulatory pathology. Of particular importance, future use of SR will provide an effective method for assessing potential therapeutic treatments for PAH.

pulmonary microvessels; hypoxia; intact chest; rat

ALVEOLAR HYPOXIA, A POTENTIAL adverse complication associated with numerous respiratory disorders, causes pulmonary vasoconstriction, which is reversible on reoxygenation. However, when sustained, the elevated shear stress within the pulmonary vasculature causes endothelial cell injury dysfunction (2), ultimately leading to the pathogenesis of pulmonary arterial hypertension (PAH). PAH is characterized by irreversible vascular remodeling and medial thickening of thin muscular-walled vessels (100–300 μm), as well as the formation of new muscle around nonmuscular or partially muscular vessels (50–150 μm) (12, 23, 24, 31). The ensuing decrease in vessel internal caliber increases pulmonary vascular resistance and, consequently, increases the workload of the heart, enhances the risk of heart failure, and is, therefore, closely associated with an increased mortality.

Several studies have indicated that the increase in pulmonary vascular resistance is further exacerbated during chronic hypoxia by a reduction in the number of perfused blood vessels within the pulmonary vascular bed, due to either vessel occlusion (i.e., extensive medial thickening) or the loss of vessels, also known as "rarefaction" or "pruning" of small vessels (8, 11, 25). More recent evidence, however, has cast doubt on this paradigm, with some reports now indicating that angiogenesis is evident within the pulmonary circulation during chronic hypoxia (13, 14, 16).

The underlying mechanisms governing the pathogenesis of PAH remain to be fully elucidated. One of the limitations in understanding the pathology of the lung has been the inability to clearly visualize blood flow within the pulmonary vascular bed. More conventional methods of assessing the vascular anatomy of the diseased lung necessitate removal of the lung from the animal (i.e., in vitro) for angiography (i.e., X-ray) or microsection analysis. Conventional angiography methods have considerable limitations in visualizing the vessels that are most susceptible to pathological changes, i.e., <200 μm (37, 40). Therefore, a technique for visualizing the pulmonary circulation within a closed-chest model, i.e., under intact neurohumoral regulation, is required to better understand the structural and functional changes in vivo and, ultimately, to assess specific treatments for lung disorders more reliably.

In a recent study, we (32) demonstrated the validity and accuracy of synchrotron radiation (SR) microangiography for visualizing pulmonary blood flow within vessels in a closed-chest rat model and for assessing dynamic changes in vessel caliber associated with acute hypoxic pulmonary vasoconstriction (HPV). Although resolution limitations of SR only enabled vessels with an internal diameter >80 μm to be visualized, many vessels that are susceptible to pathological changes during chronic hypoxia are well within the resolution capabilities of SR. In contrast to conventional angiography systems, SR is characterized by high brilliance and extreme collimation (36), allowing enhanced sensitivity to contrast material and superior image quality in terms of spatial and density resolution because divergence and scatter of X-ray photons are eliminated.

The primary aim of this study was to utilize SR microangiography to effectively highlight changes in pulmonary blood flow

Address for reprint requests and other correspondence: D. O. Schwenke, Dept. of Physiology, Univ. of Otago, PO Box 56, Dunedin, New Zealand (e-mail: daryl.schwenke@stonebow.otago.ac.nz).

The costs of publication of this article were defrayed in part by the payment of page charges. The article must therefore be hereby marked "*advertisement*" in accordance with 18 U.S.C. Section 1734 solely to indicate this fact.

distribution, following the pathogenesis of chronic hypoxia-induced PAH. Because of the resolution limitations of SR, we only assessed those pulmonary arterioles with an internal diameter >80 μm. The structural changes in the pulmonary circulation associated with chronic hypoxia have been shown to alter the functional properties of the pulmonary vasculature, in particular, the vasoconstriction response to acute hypoxia (i.e., HPV) (19, 22). This altered HPV has been attributed, at least in part, to the modulatory effects of the sympathetic nervous system on the pulmonary vasculature (33, 35). Therefore, we also aimed to utilize the high definition of SR to assess the adverse changes in pulmonary reactivity to acute hypoxia and, furthermore, to distinguish the local intrinsic response (i.e., HPV) from that of the extrinsic neural response (i.e., sympathetic modulation) by using propranolol to inhibit β-adrenoceptor activation.

MATERIALS AND METHODS

Animals. Experiments were conducted on 10 male Sprague-Dawley rats (10 wk old; ~220–320 g body wt). All rats were on a 12:12-h light-dark cycle at 25 ± 1°C and were provided with food and water ad libitum. Rats were housed in standard normoxic conditions (n = 5) or were continuously housed in a hypoxic chamber (10 ± 0.1% O_2) for 4 wk (n = 5), except for a 10-min interval each day when the chamber was cleaned. The hypoxic gas mixture was prepared from N_2 (gas cylinders) and compressed air and was continuously delivered to the hypoxic chamber (30 liter capacity) at a flow rate of ~8 l/min. All experiments were approved by the local Animal Ethics Committee and conducted in accordance with the guidelines of the Physiological Society of Japan.

Anesthesia and surgical preparation. Rats were anesthetized with pentobarbital sodium (60 mg/kg ip). Supplementary doses of anesthetic were periodically administered (~15 $mg \cdot kg^{-1} \cdot h^{-1}$ ip). Throughout the experimental protocol, body temperature was maintained at 37°C using a rectal thermistor coupled with a thermostatically controlled heating pad.

The trachea was cannulated, and the lungs were ventilated with a rodent ventilator (SN-480-7; Shinano, Tokyo, Japan). The inspirate gas was enriched with O_2 (~50% O_2), and the ventilator settings were adjusted (tidal volume ~3.5 ml; frequency of ~70 /min). A femoral artery and vein were cannulated for measurement of systemic arterial blood pressure (ABP) and drug administration, respectively. A 20-gauge BD Angiocath catheter (Becton Dickinson), with the tip at a 30-degree angle, was inserted into the jugular vein and advanced into the right ventricle for administering contrast agent and intermittently measuring right ventricular pressure (RVP).

The rat was securely fastened to a clear Perspex surgical plate, which had a single window opening directly beneath the thorax area. The surgical plate was then fixed in a vertical position in front of the beam pathway, so that the synchrotron beam could pass perpendicular to the sagittal plane from anterior to posterior through the rat thorax and ultimately to a SATICON X-ray camera described below.

Microangiographic system. The pulmonary circulation was visualized with SR microangiography at the SPring-8 BL28B2 beam-line facility (Hyogo, Japan). The use of SR for visualizing the pulmonary microcirculation in the closed-chest rat has previously been described in detail (32).

In brief, SR has a broad and continuous spectrum from the infrared to the X-ray regions. A single crystal monochromator was used to select a single energy of SR, producing X-rays of a very narrow energy bandwidth for imaging. This SR system comprised a monochromatic 33.2-keV X-ray source, just above the iodine K-edge energy for maximal contrast.

X-rays transmitted through the rats were detected by an X-ray detector (Hitachi Denshi Techno-System, Tokyo, Japan) incorporating a SATICON X-ray pickup tube (Hamamatsu Photonics, Shizuoka, Japan). The biomedical imaging SATICON X-ray camera has a resolution of 1,050 scanning lines and can record images at a maximum speed of 30 frames/s for up to 30 s. The shutter open time used in this study was 2.6–3.0 ms/frame. The detector features a 9.5-μm equivalent pixel size projected onto the input area and an input field size of 9.5 × 9.5 mm. High-resolution images were stored in a digital frame memory system with 1,024 × 1,024 pixel format and 10-bit resolution.

Experimental protocol. The rat was positioned in front of the beam line so that the upper segment of the left lobe was positioned in front of the SATICON X-ray camera in alignment with the 9.5 × 9.5-mm imaging field (i.e., between the 2nd and 3rd rib; Fig. 1). Subsequently, baseline heart rate (HR), RVP, and ABP data were collected. Immediately before vessels were imaged, the three-way stopcock on the right ventricle catheter was opened to a clinical autoinjector (Nemoto Kyorindo, Tokyo, Japan), which was used to inject a single bolus of contrast agent (Iomeron 350; Eisai, Tokyo, Japan) at high speed (0.4 ml/s). For each 2-s period of scanning, 100 frames were recorded. Rats were given at least 10 min to recover from each injection of contrast agent. Regular inspection between contrast injections confirmed that the pulmonary vasculature was clear of agent within this period of time.

After baseline imaging was completed, rats were exposed to acute hypoxia (8% O_2 in N_2) for 4 min. During acute hypoxia, ABP, HR, and RVP data were continuously recorded until the 3rd min, after which recording of RVP was stopped, and the catheter was switched from the pressure transducer to the clinical injector for imaging. Lung microangiography was performed on the hypoxic lung after the 4th min of hypoxia.

After recovery from the acute hypoxic test, rats were administered the β-receptor blocker propranolol (2 mg/kg iv). After 10–15 min was allowed for all cardiovascular variables to stabilize, pulmonary microangiography was repeated before and after acute hypoxia.

Data acquisition and analysis. The RVP and ABP signals were detected by separate Deltran pressure transducers (Utah Medical Products), and the signals were relayed to PowerLab bridge amplifiers (ML117, ADInstruments) and then continuously sampled at 500 Hz with an eight-channel MacLab/8s interface hardware system (ADInstruments) and recorded on a Macintosh Power Book G4 using Chart software (version 5.0.1, ADInstruments). HR was derived from the arterial systolic peaks.

From the 2-s period of image collection, one frame per scan (one scan = 100 frames) was selected for image enhancement and analysis. Furthermore, only those frames recorded at, or near, end systole were used for assessing and comparing pulmonary vessel diameter between baseline and hypoxic conditions.

All imaged vessel branches were counted. Where possible, the widths of two to four vessels of each branching generation (2nd to 4th

Fig. 1. A schematic drawing of the arterial circulation of the left lung in a rat. The square box represents the position of the 9.5 × 9.5-mm imaging window used for microangiography of the pulmonary microvessels. [Reprinted from Schwenke et al. (32).]

generation) were measured to ensure that a wide variety of vessel sizes was selected from each frame. Vessels were categorized according to internal diameter: 100–200, 200–300, 300–500, and >500 μm. The internal diameter of individual vessels was measured before and after acute hypoxia, with and without β-receptor blockade (i.e., propranolol treatment).

Image analysis. The computer-imaging program Image Pro-plus (version 4.1, Media Cybernetics) was used to enhance the contrast and clarity of angiogram images. To enhance images, a temporal subtraction operation was performed for flat-field correction using summation results of 10 consecutive frames acquired before contrast agent injection. The summation image taken before injection was subtracted from a single raw image taken after injection to eliminate the superimposed background structure.

Image Pro-plus was also used to evaluate the vessel internal diameter. A 100-μm-thick tungsten filament, which had been placed directly across the corner of the detector's window, appeared in all of the recorded images and was subsequently used as a reference for calculating vessel diameter (μm). The line-profile function of Image Pro-plus was used to measure changes in pixel intensity (brightness) along manually drawn segments spanning 10–40 pixels on either side in the direction perpendicular to the vessel (see Fig. 2). The first edge of the vessel was determined as the pixel at which intensity decreased by 1.5 standard deviations below that of the preceding 10–40 pixels (depending on space between vessels). The opposite criterion was applied to ascertain the distal edge of the vessel. This boundary segmentation procedure was performed at two different points along the length of the vessel, and the average of the two values was used for data collation. To assess reproducibility, the procedure for measuring vessel width was repeated by a second observer. Of the total number of vessels analyzed (91 vessels from normoxic and chronic hypoxic rats; see RESULTS), 50 vessels from various branching generations were randomly selected from the appropriate angiograph image for analyses by a second observer. The value for each vessel width that was analyzed by both observers was highly reproducible. Regression analysis indicated that the measurements from both observers were highly correlated ($y = 6.752 + 0.983x$, $r^2 = 0.975$) and had an average difference of 6 ± 3 μm (for 100- to 200-μm vessels) to 9 ± 4 μm (for 300–500 μm).

Evaluation of accuracy of measurement. We (32) have previously described in detail the method of evaluating the accuracy of measurement. In brief, we estimated a margin of error for detecting the edge of a vessel by assessing pixel variability of the reference wire (known diameter of 100 μm). Before commencing the study, we measured wire width at 40 random points along its length. The mean width of this reference wire was 12.99 pixels (SD ± 1.12). This equates to an average pixel size of 7.69 μm (95% confidence interval of 7.496–7.908 μm). Consequently, the 100-μm tungsten wire could accurately be measured to within ~5 μm (range of 97.4–102.7 μm).

In this study, the iodine contrast agent was injected into the right ventricle so that the iodine concentration within the pulmonary circulation would have been diluted, which is likely to have attenuated X-ray absorption and potentially the accuracy of the vessel width measurement. We previously performed preliminary phantom measurements to assess the relationship between X-ray absorption and iodine concentration. The phantom measurements consisted of filling nine tubes, with an internal diameter of 200 μm, with various concentrations of iodinated contrast material ranging from pure agent (370 mg/cm³) to distilled water (i.e., 0 mg/cm³). The line-profile function of Image Pro-plus was used to assess the magnitude of absorption (i.e., brightness) for each concentration of iodinated contrast material (Fig. 2).

The widths of tubes containing an iodine concentration between 32 and 370 mg/cm³ could be accurately measured with a small margin of error, e.g., the width of the tube containing 32 mg/cm³ iodine was measured at 40 points and had a 95% confidence interval of 196.84–203.26 μm. This is a margin of error similar to that obtained for multiple measurements of the tungsten reference wire.

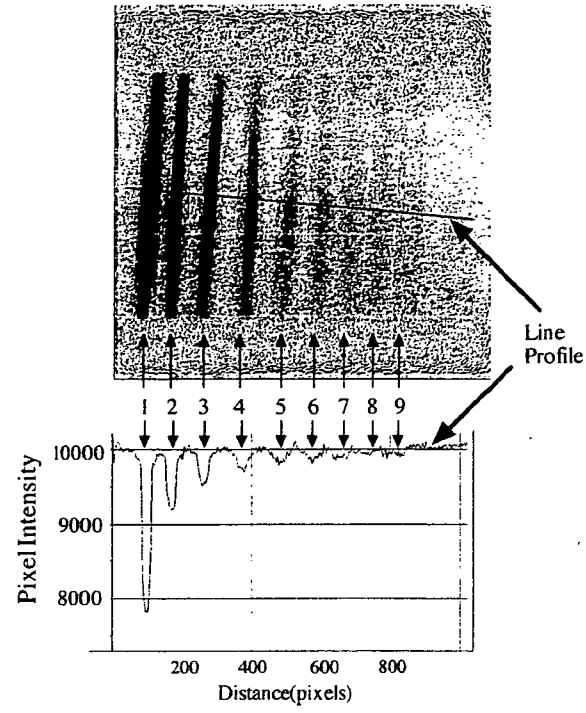

Fig. 2. *Top*: an angiograph image obtained from a phantom study that assessed X-ray absorption of 9 tubes containing *1*) Iopamiron 370 (370 mg/cm³ iodine; Nihon Schering), *2*) 127 mg/cm³ iodine (diluted contrast material with distilled water), *3*) 64 mg/cm³ iodine, *4*) 32 mg/cm³ iodine, *5*) 12.8 mg/cm³ iodine, *6*) 6.4 mg/cm³ iodine, *7*) 1.28 mg/cm³ iodine, *8*) distilled water, and *9*) air. A 5-mm-thick aluminum mask was overlaid to simulate attenuation by the animal body. Concentrations ranging from 32 to 127 mg/cm³ of iodine simulate typical in vivo conditions for intra-arterial injection techniques. *Bottom*: computerized line profile (representing the solid line transecting all 9 tubes in *top*) was performed to show that changes in pixel intensity (i.e., brightness), which reflect the magnitude of absorption, are dependent on iodine concentration.

These results show that measurements of 200 μm in diameter can be made precisely for those vessels with an iodine concentration of >32 mg/cm³. Moreover, it seems reasonable to suppose that measurements of ~100 μm in diameter can be made with the required precision for those vessels with an iodine concentration of 64 mg/cm³ or greater.

Statistical analysis. All statistical analyses were conducted with Statview (version 5.01; SAS Institute). All results are presented as means ± SE. Two-way ANOVA (repeated measures) was used to test whether propranolol significantly altered the dynamic pulmonary vasoconstriction response to acute hypoxia. One-way ANOVA (factorial) was used to test for differences in *1*) vessel caliber during normoxia and acute hypoxia and *2*) baseline values for normoxic rats (N-rats) compared with chronic hypoxic rats (CH-rats). Where statistical significance was reached, post hoc analyses were incorporated using the paired or unpaired *t*-test with the Dunnett's correction for multiple comparisons. A P value ≤0.05 was predetermined as the level of significance for all statistical analysis.

RESULTS

Baseline. Rats had an initial body weight of ~285 g before being placed into a normoxic (N-rats) or hypoxic chamber (CH-rats) for 4 wk. The gain in body weight of CH-rats (~20%

increase) was significantly lower ($P < 0.01$) than that for N-rats (~74% increase) over the 4-wk period. Chronic hypoxia induced PAH (see Table 1), as demonstrated by our observation that systolic RVP of CH-rats was ~120% higher than that of N-rats ($P < 0.01$). Chronic hypoxia did not significantly alter mean ABP (MABP) or HR.

Using SR, we were able to clearly visualize the blood flow of pulmonary microvessels (>80 μm) in the left lung of both N-rats and CH-rats. The typical branching pattern of the pulmonary circulation from the main axial artery of the left lobe to the fourth generation of branching (within the 9.5 × 9.5 mm imaging window) of a N-rat and a CH-rat is presented below (see Fig. 4).

The internal diameter of 52 vessels was measured in five N-rats: 24 vessels with a diameter between 100 and 200 μm, 15 vessels with a diameter between 200 and 300 μm, 7 vessels with a diameter between 300 and 500 μm, and 6 vessels with a diameter >500 μm. In comparison, CH-rats had comparatively fewer vessels (Fig. 3*A*); thus the internal diameter of 39 vessels was measured in five CH-rats: 15 vessels with a diameter between 100 and 200 μm, 10 vessels with a diameter between 200 and 300 μm, 7 vessels with a diameter between 300 and 500 μm, and 7 vessels with a diameter >500 μm.

The total number of vessel branches visible within each baseline image (i.e., 9.5 × 9.5-mm imaging window) was counted. As illustrated in Fig. 3*A*, the number of opaque third- and fourth-generation vessels for CH-rats (9 ± 1 and 16 ± 2 vessels, respectively) was significantly fewer than the number for N-rats (14 ± 1 and 30 ± 2 vessels, respectively; $P < 0.05$). The numbers of first- and second-generation branches were not significantly different between N-rats and CH-rats (2 and 4 or 5, respectively).

Vessel caliber tended to decrease according to each generation of branching, as well as the distance away from the main axial artery toward the periphery (Fig. 3*B*). However, often more than one size category could be found within one branching generation. For example, the third generation of branching (135–290 μm) comprised vessels of the 100- to 200-μm and 200- to 300-μm categories (Fig. 3*B*). The internal diameter of the first-generation branch in CH-rats (740 ± 53 μm) was significantly larger than that shown in N-rats (511 ± 57 μm; $P < 0.05$), possibly because of the higher distending pressure (i.e., pulmonary arterial pressure) for CH-rats. Vessel caliber

Table 1. *Systolic RVP, MABP, and HR data of anesthetized N-rats and CH-rats before and after propranolol administration*

	Systolic RVP, mmHg	MABP, mmHg	HR, beats/min
	Saline		
N-rats	24.3±1.0	103±7	338±13
CH-rats	53.1±2.0†	118±4	353±13
	Propranolol (2 mg/kg iv)		
N-rats	27.3±1.4	105±6	319±4
CH-rats	54.2±1.7†	136±3*†	294±5*†

Values are means ± SE. N-rats, normoxic rats ($n = 5$); CH-rats, chronic hypoxic rats ($n = 5$); RVP, right ventricular pressure; MABP, mean arterial blood pressure; HR, heart rate. *Significant difference between saline and propranolol ($P < 0.01$). †Significant difference between N-rats and CH-rats ($P < 0.01$).

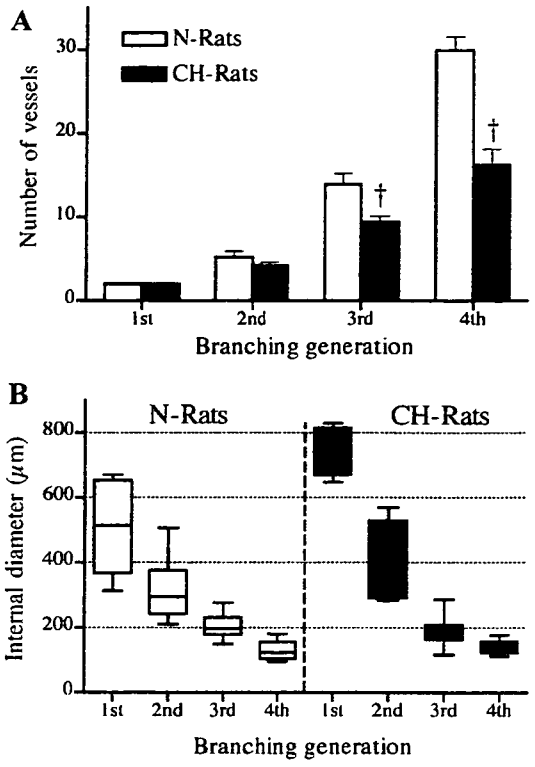

Fig. 3. Changes in the number of opaque vessels (means ± SE) (*A*) and range of vessel sizes (box and whisker graph; *B*) at each of the first 4 branching generations of the pulmonary circulation in normoxic rats (N-rats; $n = 5$) and chronic hypoxic rats (CH-rats; $n = 5$). †Significant difference between N-rats and CH-rats ($P < 0.05$).

was not significantly different between N-rats and CH-rats for the second generation (210–570 μm), third generation (135–290 μm), and fourth generation of branching (90–180 μm) (Fig. 3*B*).

Responses to acute hypoxia. N-rats and CH-rats were exposed to 8% O_2 for 4 min. Acute hypoxia caused a significant decrease in the internal diameter of all vessels with an internal diameter <500 μm (for N-rats) or <300 μm (for CH-rats) (Figs. 4 and 5). In both groups of rats, the magnitude of constriction tended to increase as vessel caliber decreased, with the greatest degree of vasoconstriction occurring in those vessels with a diameter between 100 and 300 μm. These vessels were generally of the third to fourth generation of branching. There was no significant difference between N-rats and CH-rats regarding the magnitude of HPV for all vessel sizes.

The magnitudes of responses to hypoxia for systolic RVP, MABP, and HR are presented in Fig. 6. Acute hypoxia induced a significant 21% increase in systolic RVP ($P < 0.01$) in N-rats, which was not significantly different from that observed in CH-rats (27% increase above baseline). This increase in systolic RVP reflects the HPV seen with microangiography. Hypoxia decreased MABP in CH-rats, but significantly more so in N-rats (40% and 54% decrease, respectively). Hypoxia did not alter HR in either N-rats or CH-rats.

Responses to propranolol. N-rats and CH-rats were administered the β-receptor blocker propranolol (2 mg/kg iv). Propranolol did not significantly alter baseline pulmonary vessel

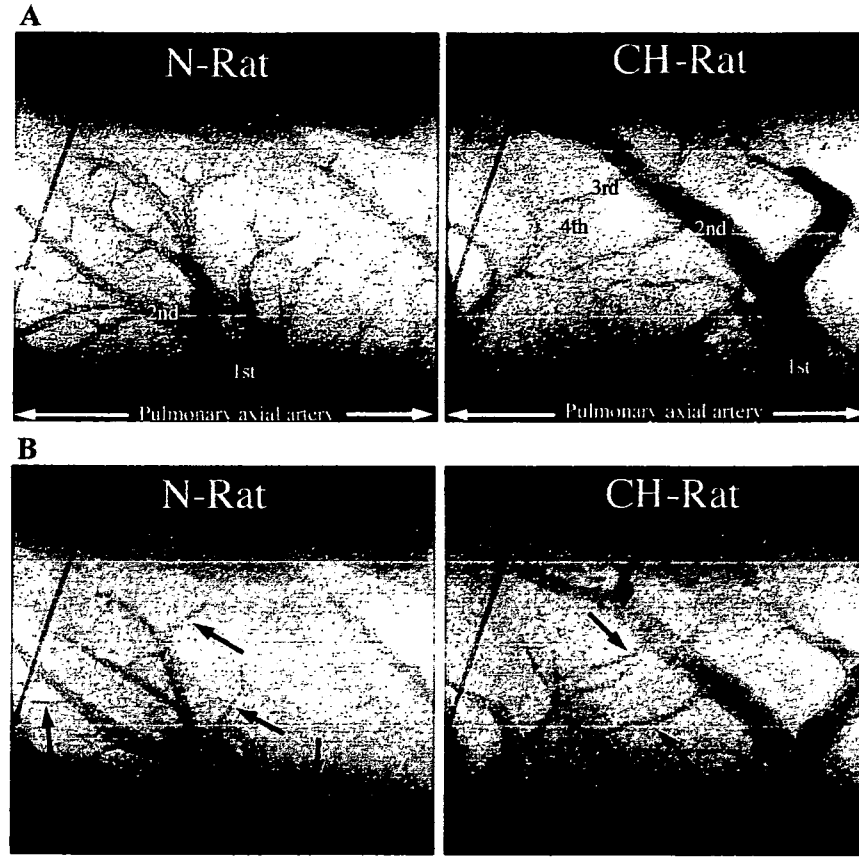

Fig. 4. Typical microangiogram images showing the branching pattern of small pulmonary arteries in N-rats (n = 5) and CH-rats (n = 5). Pulmonary branches to the 4th generation from the left main axial artery (not in the image) were visible. The tungsten wire in the *top left* of each image is a reference of 100 μm diameter. Images were recorded during air breathing (*A*) and after 4 min of acute hypoxia (8% O_2; *B*). Images for *A* and *B* were obtained from the same respective N-rat or CH-rat. The black arrows point to branches of the pulmonary vessels that have constricted in response to hypoxia.

caliber for any of the vessel size groups analyzed, in both N-rats and CH-rats. The lack of effect of propranolol on pulmonary vessel caliber for N-rats and CH-rats was reflected in the insignificant response of systolic RVP to propranolol (Table 1). In N-rats, propranolol did not significantly alter MABP or HR. In CH-rats, propranolol significantly increased MABP (15% increase) and caused a 17% decrease in HR ($P < 0.01$).

In N-rats, β-receptor blockade significantly exacerbated the magnitude of acute hypoxic vasoconstriction in 200- to 300-μm-sized pulmonary vessels (Fig. 5). However, the systolic RVP, MABP, and HR responses to acute hypoxia were unaltered (Fig. 6). In comparison, β-receptor blockade in CH-rats significantly accentuated the systolic RVP response to acute hypoxia ($P < 0.05$), reflecting extensive pulmonary vasoconstriction in 200- to 300-μm-sized vessels and, unlike that observed for N-rats, even greater constriction in 100- to 200-μm-sized vessels (Fig. 5). The HPV response of vessels with a caliber >300 μm was not altered by β-receptor blockade in N-rats or CH-rats.

DISCUSSION

This study has demonstrated the effectiveness of SR for visualizing the adverse anatomic and functional changes of the pulmonary circulation associated with the pathogenesis of pulmonary hypertension in a closed-chest rat model.

PAH. Although significant advances in the treatment of pulmonary disorders have been made in recent decades, the

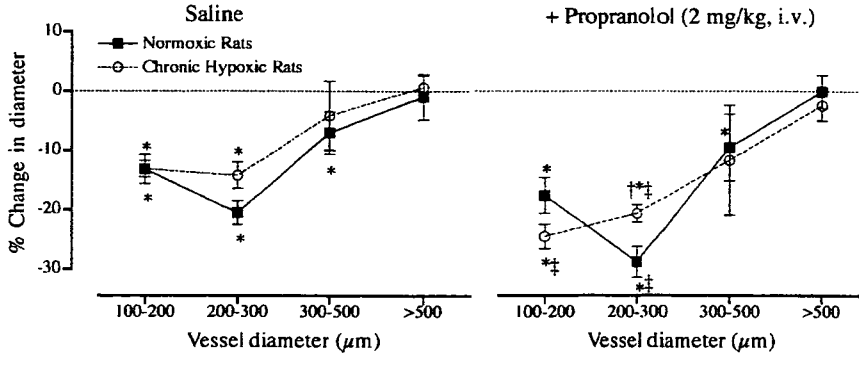

Fig. 5. Relationship between vessel size and the magnitude of pulmonary vasoconstriction (%decrease in vessel diameter) in response to acute hypoxia (8% O_2 for 4 min) in N-rats (n = 5) and CH-rats (n = 5) before (*left*) and after (*right*) intravenous administration of propranolol (2 mg/kg). *Significant vasoconstriction response to acute hypoxia ($P < 0.05$). †Significant difference between N-rats and CH-rats ($P < 0.05$). ‡Significant change in the magnitude of vasoconstriction after propranolol administration ($P < 0.05$).

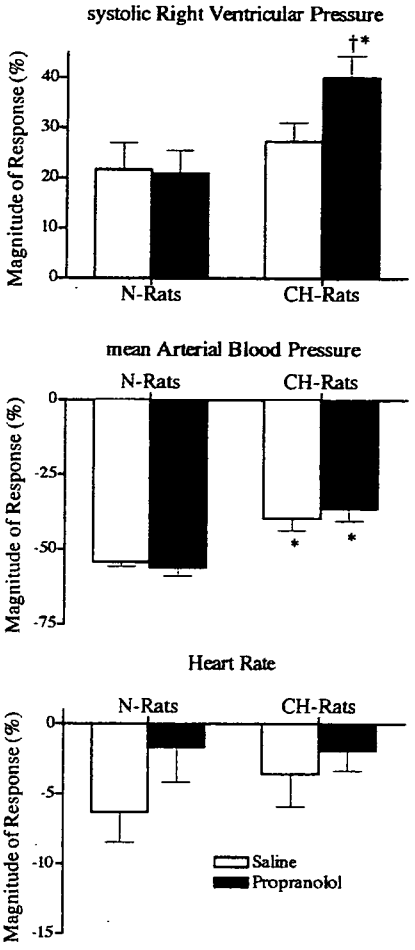

Fig. 6. Hemodynamic responses (% change) of N-rats (n = 5) and CH-rats (n = 5) to acute hypoxia (8% O_2 for 4 min) before and after intravenous administration of propranolol (2 mg/kg). *Significant difference in the magnitude of response between N-rats and CH-rats ($P < 0.05$). †Significant response to propranolol ($P < 0.01$).

underlying mechanisms governing the pathogenesis of PAH remain to be fully elucidated. Specifically, anatomic and structural changes within the pulmonary vascular bed during chronic hypoxia remain unclear.

On the basis of the early work of Reid and colleagues (8, 11, 12, 25), it had become accepted that a reduction in the number of perfused vessels within the pulmonary circulation was an important structural pathology that contributed to the sustained increase in vascular resistance during the pathogenesis of PAH. The reduction in perfused vessels was attributed to either the encroachment of smooth muscle into the vessel lumen, thereby occluding blood flow, or by a reduction in the total number of vessels (i.e., pruning).

One limitation of these studies was the inability to clearly identify the region of susceptibility and the degree of pruning or reduced perfusion. Indeed, because of the limited resolution of conventional X-ray systems, the lung had to first be excised for angiography and then pruning was nonquantitatively described from crude angiographs as a decrease in "background haze" or "background filling" (representing small peripheral vessels) (11, 21, 30).

We (32) have previously described the high definition achieved with SR microangiography for visualizing pulmonary microvessels, with an internal diameter >80 μm. In this study, using SR, we were able to confirm that exposure to chronic hypoxia for 4 wk reduced the number of opaque arterioles with internal diameter >80 μm within the pulmonary circulation. Unlike previous studies, this study was also able to identify the region of susceptibility (i.e., third to fourth generation of branching, 100–300 μm) and to quantify the degree of change (e.g., CH-rats had 47% fewer opaque vessels of the third generation than N-rats) within a closed-chest model, i.e., under intact neurohumoral regulation. One significant limitation with SR, however, is that it is not possible to determine whether the reduction in the number of opaque vessels is due to *1*) pruning of vessels, *2*) occlusion of existing vessels (i.e., complete encroachment of smooth muscle within the vessel lumen), or *3*) partial occlusion, reducing the internal diameter below the resolution limit of SR (i.e., 80 μm).

In the latter case, vessels would still be perfused but would not be visualized by SR. Consequently, the change in the number of perfused microvessels could potentially be overestimated, since we were unable to distinguish between completely occluded and partially occluded vessels. Without further improvements in the signal-to-noise ratio of pixel areas containing fifth-generation branches, it is presently not possible to quantify to what extent the microvessels are perfused in the CH-rat model.

The lung is one of the most densely vascularized organs; therefore, it is extremely difficult to accurately quantify the number of vessels within the "whole" lung. Some studies have claimed that casting techniques, which apply a high-perfusion pressure to distend and fill all arteries to the level of the capillaries, provides evidence that chronic hypoxic reduces vessel number, supporting the concept of pruning (11, 30). However, the reduction of the number of vessels filled with medium within a cast may simply be the result of occlusion, rather than the loss of vessels.

In the past 5 yr, the paradigm of vessel pruning during chronic hypoxia has been challenged, with some reports indicating that the pulmonary circulation appears to undergo angiogenesis during chronic hypoxia (13, 14, 16). However, the vascular region of angiogenesis is uncertain but is likely to occur (if at all) within the capillary bed and/or venules (not the arterioles) because these are the regions of angiogenesis within the systemic circulation (6, 28, 29). Unfortunately, visualizing the capillary network of the lung is presently beyond the resolution capabilities of SR with iodinized contrast agents.

Limitations of this study. Our group has previously described the limitations of SR for visualizing pulmonary vessels <80 μm but also reported that, despite this limitation, a majority of vessels that are susceptible to pathological disorders, and that significantly contribute to an increase in vascular resistance, generally have an internal diameter between 50 and <300 μm (11, 32, 37, 40), i.e., resistance vessels that are at least partially muscular (12). However, resistance vessels <70 μm and lacking complete muscular media also constrict in response to hypoxia (10, 27) and therefore are also likely to be susceptible to pathological changes.

When analyzing the vasoconstriction response to acute hypoxia, we could only analyze vessels with an internal caliber >100 μm because vasoconstriction of vessels <100 μm re-

duced their caliber below the resolution capabilities of SR (i.e., <80 μm).

Another significant limitation of this study is the inability of SR to assess the integrity of the pulmonary arterial vascular wall. Numerous studies have reported that pulmonary vascular remodeling and medial thickening during chronic exposure are significant structural pathologies responsible for the increase in vascular resistance (12, 23, 24, 31). Assessment of vascular remodeling often necessitates histochemical analysis. On the other hand, SR is only able to measure the internal diameter of perfused vessels (assuming the vessel contains sufficient contrast medium) and is therefore a simple, albeit useful, method for assessing gross anatomic changes in the pulmonary circulation of the hypertensive lung. Important information concerning vascular wall thickness and medial thickening cannot be assessed with SR.

In this study, we could not view the circulation of the whole lung; rather, we were restricted to a relatively small field of view of 9.5 × 9.5 mm. We therefore make the assumption that the image captured within the 9 × 9 window is representative of the whole lung circulation. However, changes in vascular resistance (during either acute of chronic hypoxia) are the consequence of global pulmonary vasoconstriction and/or remodeling.

HPV in the rat. In this study, we used SR to assess the dynamic changes in vessel caliber during acute hypoxia (i.e., HPV). The results of this study concur with our previous report (32) that showed, in N-rats, that all vessels with a diameter <500 μm, especially between 200 and 300 μm, constricted in response to acute hypoxia (8% O_2). The unique result of this study is that chronic hypoxia did not significantly alter HPV, as assessed by hemodynamic and microangiography analysis.

HPV has been reported to preferentially occur in vessels with an internal diameter of ~150–300 μm in cats and rabbits (17, 34, 35) and rats (32) and up to 600 μm in dogs (1). Chronic hypoxia has been reported to alter acute HPV due to structural changes in the pulmonary vasculature (22). According to the literature, chronic hypoxia can potentially attenuate (9, 15, 38, 41), enhance, or have no effect on the acute HPV (5, 7, 18). Despite decades of research concerning HPV, the exact mechanism(s) that governs acute HPV is yet to be fully elucidated, although various humoral (e.g., nitric oxide) and neural pathways are likely to be involved [see Moudgil et al. (26) for a review]. In this study, we aimed to specifically assess sympathetic modulation of the HPV by SR microangiography. Although sympathetic fibers innervate the pulmonary vasculature, neural control of "tonic" pulmonary vascular tone is less prominent than that of the systemic vasculature. However, modulation of the pulmonary vasculature by the sympathetic nervous system becomes critically important under stressful conditions, such as hypoxia (33, 35).

Hypoxia is a potent activator of pulmonary sympathetic nerve activity. The increase in sympathetic nerve activity has been reported to attenuate the local vasoconstrictor effects of hypoxia via a β-adrenoceptor-mediated vasodilator mechanism, especially when the inspired level of O_2 is ≤8% O_2 (33, 35). For example, Shirai et al. (35) reported that HPV was greater for moderate (10% O_2) than for severe hypoxia (5% O_2), but only if the hypoxia was global (i.e., whole body). If the hypoxic stimulus was restricted to just the lung (i.e., regional hypoxia), the magnitude of vasoconstriction was proportional to the degree of hypoxia (i.e., greatest for 5% O_2). Shirai et al. (35) subsequently demonstrated that the vasoconstrictor response to severe global hypoxia is offset by a sympathetic β-adrenoceptor-mediated vasodilatory mechanism.

In our study, we observed that sympathetic β-adrenoceptor blockade (using propranolol) in N-rats did not modify baseline vascular tone, but it did accentuate HPV of those vessels 200–300 μm in diameter. These results support the concept that modulation of the pulmonary vasculature by the sympathetic nervous system appears to be an important homeostatic response for limiting the magnitude of vasoconstriction under hypoxic conditions.

Interestingly, although β-adrenoceptor blockade accentuated HPV in this study, it did not significantly alter the magnitude of the systolic RVP to acute hypoxia in N-rats. This difference may be attributed to a decrease in cardiac output (not measured in this study), since β-receptor blockade has been reported to significantly reduce cardiac output (4, 20). Alternatively, the magnitude of vasoconstriction may not have been sufficient to elicit a significant change in the systolic RVP response, since *1*) propranolol accentuated the HPV of only the 200- to 300-μm vessels and *2*) the vasoconstriction observed within the 9.5 × 9.5-mm field of view may not be representative of the whole lung (as discussed above).

The mechanism(s) responsible for alterations of the HPV after chronic hypoxia remains poorly understood. In this study, we observed that β-receptor blockade in CH-rats significantly accentuated the HPV, not only in the 200- to 300-μm vessels as observed in N-rats but also in the 100- to 200-μm vessels. Consequently, the systolic RVP response to acute hypoxia was also enhanced by propranolol. These results indicate that sympathetic modulation of the HPV becomes critically enhanced after chronic hypoxia.

Although the mechanisms for these observations need to be further researched, we speculate that the enhanced HPV may be attributable to *1*) the formation of new muscle around nonmuscular or partially muscular vessels (50–150 μm) and *2*) an increase in sympathetic innervation of the pulmonary vasculature. HPV is intrinsic to the lung, and, although modulated by the endothelium, the core mechanism is in the smooth muscle cell (26). Peripheral arterioles undergo medial thickening during chronic hypoxia. Therefore, in this study, it may be possible that the potential of the 100- to 200-μm vessels to constrict was enhanced after chronic hypoxia. However, the difference in the vasoconstrictive response of 100- to 200-μm vessels between N-rats and CH-rats was only apparent after β-receptor blockade. Studies have shown that chronic hypoxia significantly increases β-receptor number within the lung (3, 39), so that modulation of HPV by the sympathetic nervous system is enhanced after chronic hypoxia. These reports are in agreement with the observations of this study.

Future directions. The primary aim of this study was to demonstrate the effectiveness of SR for "visualizing" the pathological changes in pulmonary microcirculation in a closed-chest rat model after the development of pulmonary hypertension. As a result, this study has provided a foundation with which future investigative studies can build to further elucidate the adverse changes in the pulmonary circulation during hypertension. Specifically, we used only one stimulant (acute hypoxia) to test the reactivity of the pulmonary circulation. However, the question still remains as to whether